

Self-Assembled, Ultrahigh Refractive Index Pseudo-Periodic Sn Nanostructures for Broad-Band Infrared Photon Management in Single Layer Graphene

Sidan Fu,^{#,†} Haozhe Wang,^{#,‡} Xiaoxin Wang,[†] Yi Song,[‡] Jing Kong,^{*,‡} and Jifeng Liu^{*,†}

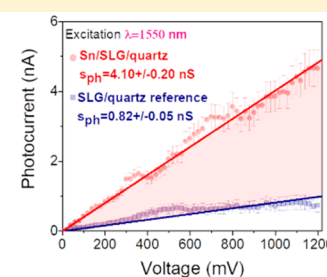
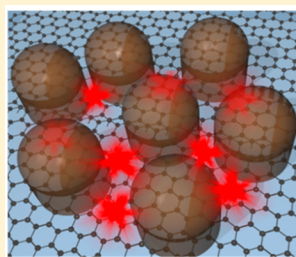
[†]Thayer School of Engineering, Dartmouth College, 14 Engineering Drive, Hanover, New Hampshire 03755, United States

[‡]Department of Electrical Engineering and Computer Science, Massachusetts Institute of Technology, 77 Massachusetts Avenue, Cambridge, Massachusetts 02139, United States

Supporting Information

ABSTRACT: Graphene is a two-dimensional material with intriguing electrical and optical properties for infrared photonic devices. However, single layer graphene (SLG) suffers from a very low optical absorption of $\sim 1\text{--}2\%$ depending on the substrate, which significantly limits its efficiency as photonic devices. In this Letter, we address this challenge by coating SLG with self-assembled, pseudoperiodic ultrahigh refractive index ($n = 8\text{--}9$ at $\lambda = 1600\text{--}5000$ nm) semimetal Sn nanostructures for highly effective, broad-band infrared photon management in SLG, offering a new approach for light trapping beyond plasmonics and high refractive index dielectric photonics. The infrared absorption in SLG on fused quartz (SiO_2) is greatly increased from $<1.5\%$ to $>15\%$ in a very broad spectral range of $\lambda = 900\text{--}2000$ nm due to the near-field electromagnetic interactions between the ultrahigh refractive index Sn nanostructures and SLG, a significant advantage over relatively narrow-band plasmonic resonances for photon management in SLG. The optical absorption enhancement in SLG has also been confirmed by field-enhanced Raman peaks from SLG and supported by higher photoconductivities both at an infrared wavelength of $\lambda = 1550$ nm and at a visible wavelength of $\lambda = 650$ nm. This work also opens the door to the investigations of ultrahigh refractive index semimetal nanostructures for nanoscale photon management.

KEYWORDS: ultrahigh refractive index semimetals, single layer graphene, infrared photon management, 2D photonic devices



Graphene is a representative of two-dimensional (2D) materials with peculiar electrical and optical properties due to the relativistic behavior of its charge carriers, as dictated by the interaction between the π electrons and the periodic potential of the hexagonal 2D lattice.^{1,2} It is especially attractive for broad-band infrared (IR) light detection due to the 0 bandgap and high carrier mobility. However, free-standing single layer graphene (SLG) only absorbs 2.3% of the incident light because of its atomic thickness and its universal optical conductivity ($e^2/4\hbar$) from the interband transitions,³ where e is the electron charge and \hbar is the reduced Planck's constant. When transferred directly onto fused quartz (SiO_2) or Si substrate for practical device applications, the absorption of SLG is further reduced as a result of increase in optical impedance mismatch.⁴ For example, when SLG is transferred to fused quartz (SiO_2) substrate, the absorption is further reduced to 1.4% according to optical transfer matrix calculations (see Figure S1 in the Supporting Information). This significantly limits its quantum efficiency for applications in free space photonic or optoelectronic devices.

Consequently, one of the open challenges for 2D photonics is how to increase the light absorption, especially over a broad spectral range, in such an atomically thin layer without

influencing the integrity of its 2D lattice. Currently, plasmonics⁵ and high refractive index dielectric nanostructures⁶ (including photonic crystals) are the two major approaches for photon management in thin absorbers. Liu et al.,⁷ Zheng et al.,⁸ and Khaleque et al.⁹ have theoretically demonstrated the possibility of increasing the absorption of graphene by involving photonic crystals. Their numerical simulation showed that the absorption of SLG can be improved by 4X. However, most investigations are limited to the calculation stage due to the relatively complicated fabrication process. Yan et al.,¹⁰ Deng et al.,¹¹ and Qin et al.¹² have reported plasmonic coupling among graphene nanopatterns to achieve an enhanced IR absorption up to 8%; however, it does break the continuity of graphene in large scale and could induce undesirable edge defects which degrade the electrical properties. On the other hand, Hashemi et al.¹³ and Lu et al.¹⁴ have theoretically illustrated the possibility of using Au or Ag plasmonic nanostructures for the same goal, which offers a relatively simple design and could potentially be applied to large scale fabrication. Liu et al.¹⁵ managed to

Received: October 1, 2018

Published: December 18, 2018

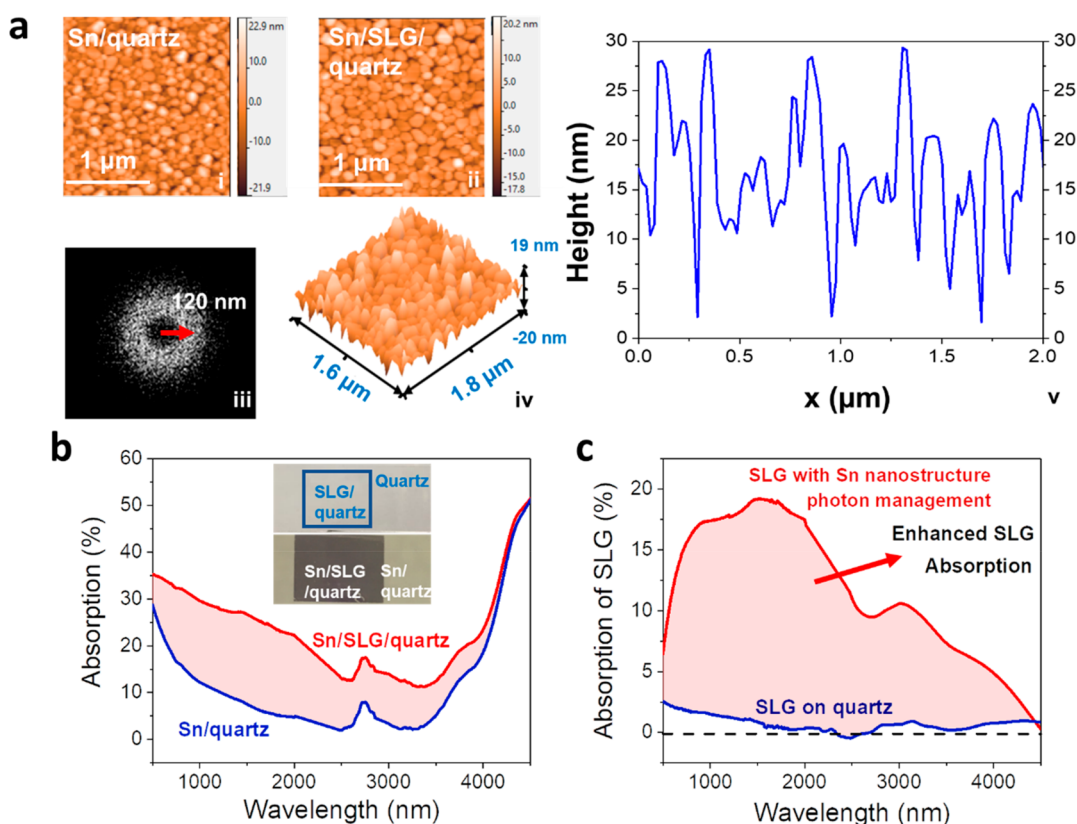


Figure 1. Atomic force microscope (AFM) images of nominally 12 nm thick Sn nanostructures on (a-i) quartz; (a-ii) SLG/quartz. Panel (a-iii) shows the Fast Fourier Transform (FFT) pattern of the AFM image in (a-ii). Panels a-iv and a-v show a three-dimensional view and a cross-sectional profile of the Sn nanostructures on SLG/quartz, respectively. (b) Absorption spectrum of the Sn nanodots/SLG/quartz region (red line) in comparison with that of the surrounding Sn nanodots/quartz region without SLG (blue line) in the wavelength range of 500–4500 nm. The peak at 2750 nm is due to the quartz substrate.^{31,32} The inset shows the photos of a pristine SLG/quartz sample (upper panel) and a SLG/quartz sample coated with 12 nm nominal thickness of Sn nanostructures (lower panel). The latter shows clear optical contrast between the regions with and without SLG. The SLG regions are $\sim 1 \times 1.5 \text{ cm}^2$ on these samples. (c) Absorption spectrum of the SLG layer in the Sn nanodots/SLG/quartz region (red line) in comparison to that of the SLG layer on quartz without Sn nanostructures (blue line). The absorption in the SLG of the Sn/SLG/quartz region is obtained by subtracting the blue curve from the red curve in (b). While most of the absorption enhancement of SLG induced by Sn nanostructures happens in the IR regime, some enhancement also occurs in visible spectral regime (i.e., 500–700 nm). This part leads to the visual contrast in the photo of the Sn/SLG/quartz sample inside (b).

transfer a layer of Au nanoparticles onto the top of graphene. Plasmonic resonance among the nanoparticles enhances the photocurrent from SLG by up to 4.5 \times at $\lambda = 520\text{--}550 \text{ nm}$ (i.e., up to 10% optical absorption in SLG), yet most of the optical absorption enhancement occurs in Au nanoparticles instead of in graphene. In fact, enhanced photocurrent in 2D photonic devices via photon management over a broad spectral bandwidth of $>100 \text{ nm}$ has rarely been demonstrated, meaning that the broad-band absorption of SLG is far from being fully utilized. Besides, the relatively narrow and sharp plasmonic resonances of Au and Ag nanoparticles, which locate mostly in the visible light regime, are not preferable for broad-band IR photonic applications such as IR photodetectors/image sensors and thermophotovoltaic (TPV) cells.¹⁶

In this Letter, we present self-assembled, ultrahigh refractive index semimetal Sn nanostructures ($n = 8\text{--}9$ at $\lambda = 1600\text{--}5000 \text{ nm}$) for highly efficient, broad-band IR photon management in SLG, offering a new light trapping approach beyond plasmonics and high refractive index dielectric photonics. Sn has a low melting point of 504 K,¹⁷ which facilitates low-temperature self-assembly of pseudoperiodic nanostructures on various substrates via surface diffusion and dewetting without the need of sophisticated nanolithography.

Thanks to the photon management contributed by these ultrahigh refractive index Sn nanostructures, $>15\%$ IR absorption is achieved from the SLG layer in a broad spectral range of $\lambda = 900\text{--}2000 \text{ nm}$, a significant advantage over the narrow-band plasmonic resonators. Moreover, unlike Au and Ag that are incompatible with large-scale microfabrication in foundries due to deep level defect centers, alloying Si and Ge with Sn (all being Group IV elements) has recently become a hot topic for advanced Complementary Metal Oxide Semiconductor (CMOS) technology.¹⁸ The highly effective photon management in SLG and the facile/scalable fabrication process could both significantly benefit the future development of 2D photonics and optoelectronics. This work also opens the door to the investigations of other ultrahigh refractive index semimetal nanostructures, such as Bi¹⁹ and Sb,²⁰ for nanoscale photon management.

RESULTS AND DISCUSSION

Principles and Advantages of Ultrahigh Refractive Index Semimetal Nanostructures for Photon Management. From a refractive index point of view, we can consider existing plasmonics and high refractive index dielectrics structures as two extremes. For plasmonics, materials with k

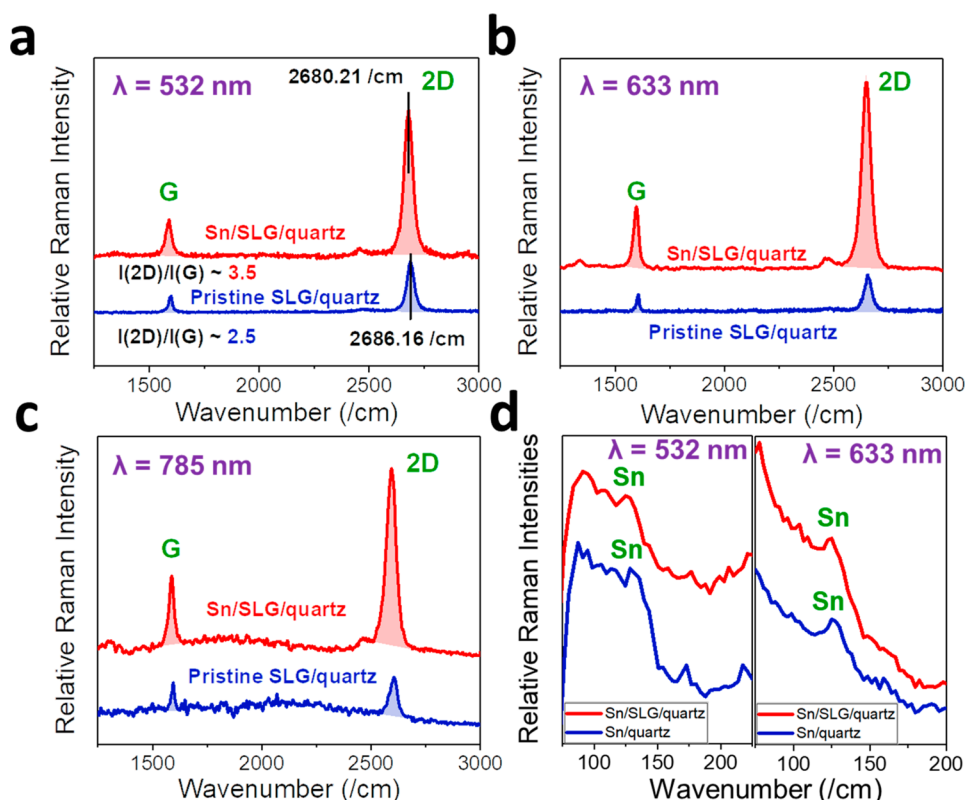


Figure 2. Raman spectra of SLG under the pseudoperiodic Sn nanostructures in comparison with those of the pristine SLG on quartz at excitation wavelengths of (a) 532, (b) 633, and (c) 785 nm. The red and blue shaded areas correspond to the integrated Raman intensities of 2D and G bands in the Sn/SLG/quartz sample and the pristine SLG/quartz sample, respectively. Quantitative analyses of the field-enhanced Raman peak intensities are summarized in Table 1. Panel (d) shows the Raman spectra of β -Sn nanostructures on SLG/quartz in comparison with those directly deposited on quartz at excitation wavelengths of 532 nm (left panel) and 633 nm (right panel). There is no enhancement in the Sn Raman peak intensity, further assuring that the enhanced absorption in the Sn/SLG/quartz region compared to the Sn/quartz region (shown in Figure 1b) is attributed to the SLG layer as a result of the photon management.

$\gg n$ are applied, where n and k are the real part and the imaginary part of the refractive index, respectively (k is also known as “extinction coefficient”). On the other hand, high refractive index dielectric materials feature $n \gg k$, with $n \sim 3$ –4 and $k \sim 0$.²¹ The light trapping strategy based on ultrahigh refractive index semimetal nanostructures, as investigated in this Letter, can be considered as an approach to optimize the optical performance between these two extremes. Particularly, it achieves a much higher refractive index ($n \sim 8$ –10) than conventional high-index dielectric materials (typically $n \leq 4$)²¹ in the near and mid-IR wavelength regime to allow much stronger field enhancement at nanoscale, thanks to an ultralarge real part of the dielectric constant of $\epsilon_1 = n^2 - k^2 > 50$. For example, β -Sn, a semimetal in Group IV of the periodic table, offers an ultrahigh refractive index of $n = 8$ –9 ($\epsilon_1 = 40$ –70) in a very broad wavelength range of $\lambda = 1600$ –5000 nm (see Figure S2 in the Supporting Information) due to the direct interband transitions.²² This property greatly enhances the scattering of the incident IR photons around the Sn nanostructures in a broad spectral regime, overcoming the challenge of relatively narrow plasmonic resonances in Au and Ag nanostructures. Indeed, we have demonstrated IR absorption enhancement in Ge IR detectors using Sn/SnO core/shell nanoneedle structures.^{23,24} The ultrahigh refractive index of Sn nanostructures can also lead to strong local field enhancement in nearby low index regions. While such an effect is similar to that of the dielectric slot waveguides reported elsewhere,^{25,26} the refractive index contrast is dramatically

increased to allow much stronger field enhancement. Due to the continuity of the electric displacement at the boundary between two media, the magnitude of the electric field at the low refractive index medium, for example, a nanoscale air gap/slot ($n = 1$) between two high index nanostructures, is greatly enhanced compared to that at the higher refractive index medium. Therefore, the optical power can be strongly concentrated into nanoscale low index regions for highly effective photon management. All these benefits make ultrahigh refractive index semimetal Sn nanostructures a promising candidate for photon management in scalable 2D IR photonic devices.

Self-Assembled, Pseudo-Periodic Sn Nanostructures.

Experimentally, Sn nanostructures are thermally evaporated onto quartz and SLG/quartz substrates. The morphologies of the nanostructures are controlled by evaporation rate and nominal thickness, as detailed in the Methods section. The morphology of the Sn nanostructures deposited on quartz and SLG/quartz are shown in the atomic force microscopy (AFM) images in Figure 1a-i and a-ii, respectively. As detailed in Figure S3 of the Supporting Information, statistically there is no difference between the morphologies of the Sn nanostructures in these two cases for 12 nm nominal thickness of Sn. The Fast Fourier Transform (FFT) pattern (Figure 1a-iii) of the AFM image in Figure 1a-ii clearly shows a ring that corresponds to an average period of 120 nm. Note that the FFT pattern is analogous to diffraction patterns, where the ring indicates an intermediate-range order of the Sn nanostructures,

Table 1. Summary of Raman Intensity Ratios of $I_{G+2D}(\text{Sn/SLG})/I_{G+2D}(\text{SLG})$ at Different Excitation Wavelengths, the Corresponding Transmittance of Raman-Scattered Photons through the Sn/SLG Nanostructures (T_{Raman}), the Estimated Field Enhancement $|E|^2/|E_0|^2$ in SLG from Eq 1, and Their Comparison with the Absorption Enhancement Measured in Figure 1c^a

excitation wavelength (nm)	Raman intensity ratio $\frac{I_{G+2D}(\text{Sn/SLG})}{I_{G+2D}(\text{SLG})}$	transmittance of Raman-scattered photons T_{Raman}	field enhancement $\frac{ E ^2}{ E_0 ^2}$	absorption enhancement
532	3.8	0.187	4.5	3.7
633	6.2	0.260	4.9	4.7
785	9.3	0.359	5.1	5.7

^aHere the Raman intensity I_{G+2D} is calculated as the integrated intensity below the G-band and the 2D band Raman peaks. The field enhancement estimated from the enhanced Raman scattering in Sn/SLG largely agrees with the absorption enhancement measurement, confirming that photon management by the Sn nanostructures is the dominant mechanism for enhanced absorption in SLG. The small discrepancy may come from the change in the doping level of SLG after Sn deposition, which modifies the relative intensities of 2D vs G band peaks.

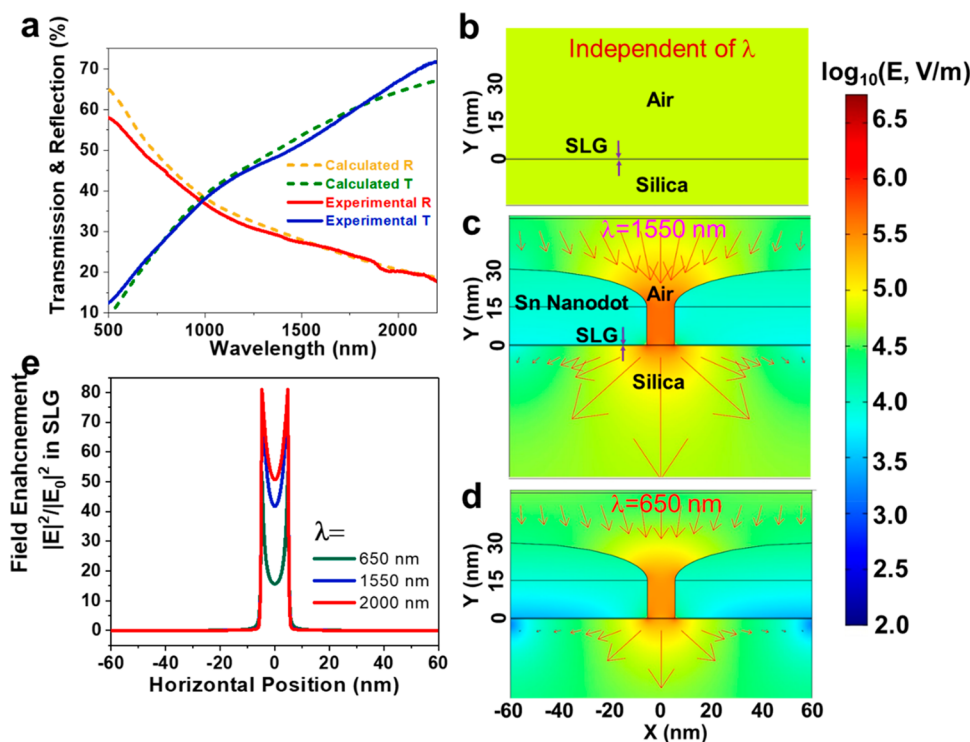


Figure 3. (a) Calculated vs experimentally measured transmittance (T) and reflectance (R) spectra from the Sn/SLG/quartz sample. The calculated data agree with the experimental results. The electric field distributions under optical excitation are shown for (b) the SLG/quartz reference, independent of wavelength; and the Sn/SLG/quartz sample at (c) $\lambda = 1550$ nm and (d) $\lambda = 650$ nm. The unit of the electric field is V/m. The red arrows indicate the directions and magnitude of the optical power flux. Panel (e) shows the field enhancement ($|E|^2/|E_0|^2$) as a function of the horizontal position in the SLG layer of the Sn/SLG/quartz sample at $\lambda = 2000$, 1550, and 650 nm. The center of the gap between Sn nanodots correspond to $x = 0$. The enhanced absorption in SLG is mainly attributed to the strong field enhancement near the gaps between pseudoperiodic Sn nanostructure.

similar to the intermediate-range atomic ordering in microcrystalline materials. Therefore, the self-assembled Sn nanostructures can be considered pseudoperiodic, which will be applied to our theoretical modeling in the later text.

Optical Absorption Spectra. The insets of Figure 1b display the photos of a pristine SLG/quartz sample (upper panel) and its counterpart coated with the pseudoperiodic Sn nanostructures (lower panel), as characterized in Figure 1a. The pristine SLG/quartz region is transparent. After Sn nanodots deposition, on the other hand, the SLG/quartz region is significantly darker than the surrounding regions on the same sample, that is, those with Sn nanodots, but no SLG. This observation clearly indicates that more light is absorbed in the Sn nanodots/SLG region than the Sn nanodots region alone.

To quantify the optical absorption (A) spectra of the samples, we measured the transmittance (T) and reflectance (R) spectra using a UV–vis–IR spectrometer and a Fourier Transform IR (FTIR) spectrometer, both equipped with integrating spheres, as detailed in the Methods. The absorption is obtained by $A = 1 - T - R$. Corresponding to the strong visual contrast on the Sn/SLG sample (see the inset of Figure 1b), 5–19% absolute increase in absorption is observed in the Sn/SLG/quartz region vs the surrounding Sn/quartz region in a broad spectral range from $\lambda = 500$ to 4000 nm (Figure 1b). Since the only difference between these two regions is the SLG (i.e., nearly no morphological difference in Sn nanostructures, as shown in Figures 1a and S3), we can consider this enhanced absorption as the effective absorption of the SLG layer with the photon management of the Sn nanostructures. The >15%

absorption in a broad near IR (NIR) spectral regime of $\lambda = 900\text{--}2000$ nm in the SLG layer of the Sn/SLG/quartz sample is significantly higher than the $\sim 1.4\%$ absorption of the SLG layer on quartz (Figure 1c). Such a strong and broad-band absorption enhancement in SLG is highly beneficial for IR photodetection.

Raman Spectroscopy Analyses and Field-Enhanced Raman Scattering from SLG. Raman spectroscopy offers more information about the optical field enhancement, doping, and quality of SLG after Sn nanostructure deposition. Since Raman scattering intensity is approximately proportional to $|E|^4$,²⁷ while optical absorption is proportional to $|E|^2$,⁵ where E is the electric field of the optical excitation wave, a stronger Raman peak intensity directly indicates field enhancement and enhanced absorption. Therefore, the significantly higher G band and 2D band Raman peaks from the SLG region of the Sn/SLG/quartz sample compared to those from the SLG/quartz reference in Figure 2a–c confirm the field enhancement and increased SLG absorption due to photon management of the Sn nanostructures. On the other hand, the Raman peak intensity of β -Sn at 125 cm^{-1} ²⁸ shows no enhancement in the Sn/SLG/quartz region compared to the Sn/quartz region (Figure 2d), indicating that there is no increase in the absorption of Sn nanostructures between these two cases. Thus, this result further assures that the optical absorption contrast between the Sn/SLG/quartz and Sn/quartz regions shown in Figure 1b is mainly due to the photon management effect in SLG.

We can further estimate the field enhancement in SLG at different Raman excitation wavelengths by comparing the integrated intensities of the G band and 2D band Raman peaks with and without Sn nanostructures, that is, evaluating the ratio of $I_{\text{G+2D}}(\text{Sn/SLG})$ to $I_{\text{G+2D}}(\text{SLG})$. Considering that the Raman-scattered photons generated in the SLG region of the Sn/SLG/quartz sample have to transmit through the SLG and the Sn nanostructures in order to be collected by the Raman spectroscopy system, we can reach the following approximation for the Raman intensity ratio of $I_{\text{G+2D}}(\text{Sn/SLG})$ to $I_{\text{G+2D}}(\text{SLG})$

$$\frac{I_{\text{G+2D}}(\text{Sn/SLG})}{I_{\text{G+2D}}(\text{SLG})} \approx \frac{|E|^4}{|E_0|^4} \cdot T_{\text{Raman}} \quad (1)$$

Here E and E_0 are the electric fields in SLG with and without Sn nanostructures, respectively, and T_{Raman} is the transmittance of the Raman-scattered photons through the Sn/SLG structures. While the transmittance of Raman-scattered photons is close to 100% for the SLG/quartz reference sample, it is dramatically reduced in Sn/SLG/quartz samples due to the enhanced absorption of SLG (Figure 1) and the scattering/absorption of the Sn nanostructures. Considering that the transmittance loss of the quartz substrate is negligibly small, T_{Raman} can be well approximated by the experimentally measured transmittance of the Sn/SLG/quartz sample at the Raman scattering wavelengths, as listed in Table 1 and further detailed in Figure 3a. Therefore, we can derive the field enhancement $|E|^2/|E_0|^2$ from eq 1, which would also be equal to the absorption enhancement in SLG theoretically. As shown Table 1, the relative field enhancements $|E|^2/|E_0|^2$ derived from Raman spectroscopy and the transmittance of the Sn/SLG/quartz sample at excitation wavelengths of $\lambda = 532, 633$, and 785 nm are indeed largely consistent with the absorption enhancement measured in Figure 1c. This result further

supports the highly effective photon management in SLG by utilizing ultrahigh refractive index Sn nanostructures. The small discrepancy between the field enhancement derived from Raman spectroscopy and the absorption enhancement from UV–vis–IR spectroscopy may be attributed to the change in the doping level of SLG after Sn deposition that modifies the Raman intensity ratio of 2D to G bands, as will be discussed next.

Raman spectroscopy can also provide the doping information on graphene, as has been calibrated to the carrier concentrations of electrically gated graphene devices.²⁹ The pristine SLG transferred to quartz substrate is p-type. The red-shift of the SLG 2D band to lower wavenumber after the deposition of Sn nanostructures (see Figures 2a and S4) indicates n-type compensation doping effect.²⁹ This compensation effect is further supported by the increase in the ratio of the 2D-band intensity to the G-band intensity, that is, $I(2\text{D})/I(\text{G})$, which increases from 2.5 to 3.5 after the deposition of Sn nanostructures. Judging from the values of $I(2\text{D})/I(\text{G})$,²⁹ we found that the SLG changes from p-type (with a hole concentration of $p \sim 5 \times 10^{12}\text{ cm}^{-2}$) to nearly intrinsic after Sn deposition.

Such a compensation doping does benefit the long wavelength IR absorption of SLG. In Figure 1c, the absorption of SLG on quartz starts to decrease and becomes very low at $\lambda > 2000$ nm due to the $5 \times 10^{12}\text{ cm}^{-2}$ p-type doping in the SLG. Since the Fermi level in p-type SLG is below the Dirac point and inside the valence band, the absorption decreases at long wavelengths due to insufficient photon energy for interband excitation from the Fermi level to the conduction band.³⁰ Specifically, using $p \sim 5 \times 10^{12}\text{ cm}^{-2}$ for pristine SLG on SiO_2 (also confirmed by Hall effect measurement), we can calculate²⁸ that the Fermi level is ~ 0.3 eV below the Dirac point in the valence band. Therefore, interband excitation is prohibited for photon energy below $\sim 2 \times 0.3\text{ eV} = 0.6\text{ eV}$. This corresponds to the wavelength range of $\lambda > 2000$ nm, which explains the low optical absorption of SLG on quartz at $\lambda > 2000$ nm. After the Sn nanodots evaporation on SLG, on the other hand, n-type compensation doping is introduced to the SLG layer, as discussed earlier. This compensation doping effect brings the Fermi level of SLG on quartz back toward the Dirac point, and therefore extends the interband IR absorption of SLG to longer wavelengths in the Sn/SLG/quartz sample. Further enhanced by the light trapping effect of Sn nanostructures, the IR absorption in the SLG layer of the Sn/SLG/quartz sample ranges from 5% to 17% at $\lambda = 2000\text{--}4000$ nm. Note that the absorption peaks at $\lambda \sim 2700$ nm and the cutoff at $\lambda > 4500$ nm are due to the IR absorption of the quartz substrate itself.^{31,32}

Finally, the Raman spectroscopy data in Figure 2 show almost no defect-related D-band signal from SLG after the deposition of Sn nanostructures, indicating that the integrity of SLG is preserved. This is a great advantage of the evaporation process compared to the sputtering process, which tends to damage the lattice of SLG and induce significant D-band in the Raman spectra.^{33,34}

Theoretical Modeling of Photon Management in SLG Using Ultrahigh Refractive Index, Pseudo-Periodic Sn Nanostructures. To understand the mechanism of photon management in the pseudoperiodic Sn nanodots/SLG structure, we also performed theoretical modeling using Wave Optics Module in COMSOL Multiphysics software, as shown in Figure 3. Based on the AFM results in Figure 1a, the

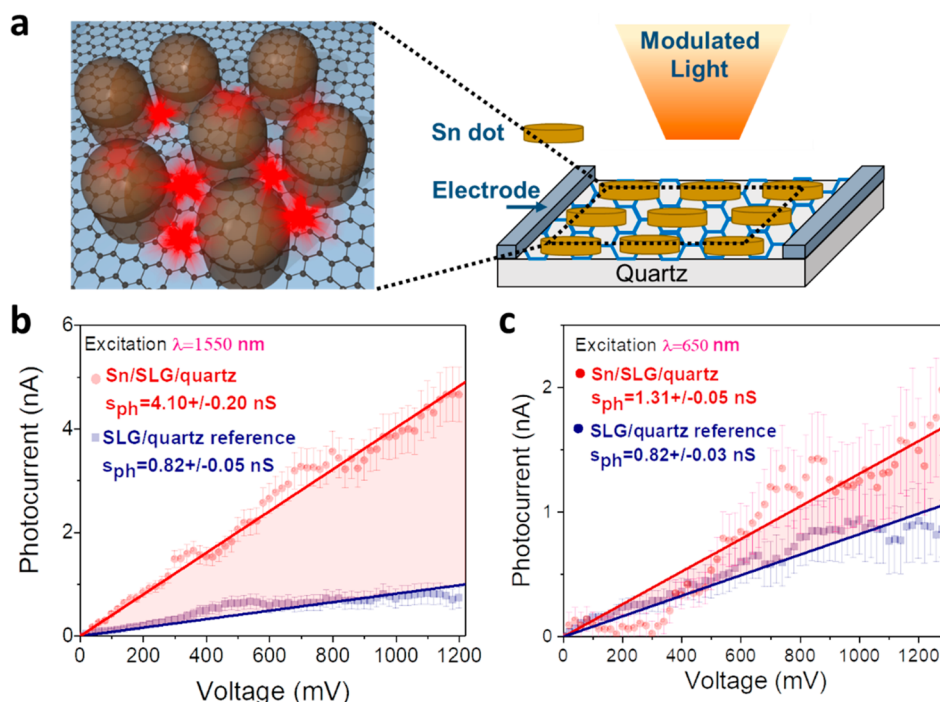


Figure 4. Photocurrent measurement on the Sn/SLG/quartz photoconductor structure. (a) Schematic experimental setup of the photocurrent measurement using an optical chopper at 300 Hz to modulate the optical excitation for a lock-in measurement. Only the photocurrent, that is, the change in current between the on and off states of the chopper, is amplified and recorded by the lock-in amplifier. The 3D schematic figure on the left illustrates a zoomed-in view of the Sn/SLG structure. This is for illustration purposes only, and the features are not drawn to scale. Photocurrent vs voltage for the Sn/SLG/quartz region in comparison with a SLG/quartz reference are shown in (b) under 1 mW IR excitation at $\lambda = 1550$ nm and (c) under 2 mW red laser excitation at $\lambda = 650$ nm.

pseudoperiodic Sn nanodots are modeled as a periodic array of “cylinder + hemi-ellipsoid dome” structures, as shown in Figure 3c,d. The validity of the periodic approximation for pseudoperiodic photonic structures has also been confirmed in previous literature when the length scale of the ordering is much greater than the wavelength of interest.^{35,36} The heights of the cylinder and the dome are both 15 nm. The diameter of the cylinder is 110 nm and the gap between the dots is 10 nm, as statistically summarized in Figure S3. As shown in Figure 3a, the calculated transmittance and reflectance spectra both agree well with the experimental results despite of the approximation of the model. Figure 3b–d further compare the calculated electric field distribution in the SLG/quartz reference (Figure 3b, wavelength-independent) with that of the Sn/SLG/quartz sample under optical excitations at $\lambda = 1550$ nm (Figure 3c) and 650 nm (Figure 3d). These data reveal that the mechanism behind the enhanced absorption in SLG is the near field electromagnetic interaction at the interface between the Sn nanodots and SLG.

As shown by the red arrows indicating the directions and magnitude of optical power flow in Figure 3c, the ultrahigh refractive index of Sn nanostructures at $\lambda = 1550$ nm ($n = 7.85$) effectively concentrates and funnels the optical power through the gaps between the Sn nanodots. Consequently, the SLG regions near the gaps experience a very strong field enhancement compared to the case without Sn nanostructures, as indicated by the red-orange high field regions in Figure 3c compared to the uniform yellow-green moderate field distribution in Figure 3b. This result confirms the slot effect and nanoscale optical confinement based on ultrahigh refractive index nanostructures, as discussed earlier. Indeed, Figure S5 in the Supporting Information shows that, when

setting $k = 0$ and keeping $n = 7.85$ for the Sn nanostructures, the optical field and the optical power flux show almost no change compared to Figure 3c. At a shorter wavelength of $\lambda = 650$ nm, the refractive index of Sn nanostructures is decreased to $n = 4.26$, leading to less effective optical power concentration and funneling through the gaps, as shown in Figure 3d. This theoretical analysis is also consistent with the trend of the optical absorption spectrum of SLG in the Sn/SLG/quartz sample shown in Figure 1c. The steep increase of absorption at $\lambda = 500$ –1000 nm in the SLG layer of the Sn/SLG/quartz sample (Figure 1c) coincides very well with the drastic increase of the refractive index (n) of Sn nanostructures (Figure S2) in the same spectral regime. This comparison further confirms that the photon management mechanism in SLG is mainly contributed by the ultrahigh refractive index of the Sn semimetal nanostructures.

As mentioned previously in Raman analyses, the absorption is proportional to $|E|^2$. Indeed, Figure 3e shows that 50–80 \times local field enhancement $|E|^2/|E_0|^2$ can be achieved in the SLG region near the gaps between the Sn nanodots at $\lambda = 2000$ nm, where E and E_0 are the electric field with and without the Sn nanostructures, respectively. As the wavelength decreases, the refractive index (n) of Sn nanodots also decreases (Figure S2), which compromises the absorption enhancement in the SLG layer (also see the comparison between Figure 3c and d). On the other hand, at long wavelengths >2500 nm, the IR absorption of the fused quartz substrate itself^{31,32} diminishes the photon management effect in SLG. The interplay of these two factors leads to a broad optimal spectral regime for SLG absorption enhancement at $\lambda = 900$ –2000 nm, with an absolute IR absorption of 16–19% from SLG. Remarkably, the 1100 nm spectral width contributed by the self-assembled

ultrahigh refractive index Sn nanostructures is $>10\times$ broader than that of the closely packed Au plasmonics gap resonator structures fabricated by extreme UV lithography,³⁷ demonstrating the unique advantages of using ultrahigh refractive index nanostructures for photon management.

Photoconductance Enhancement in SLG via Photon Management of Pseudo-Periodic Sn Nanostructures.

For optoelectronic devices such as IR photodetectors, it is interesting to check whether such an enhancement in SLG optical absorption transfers to an increase in photoresponse. Indeed, we have confirmed photoconductance enhancement from the Sn/SLG/quartz sample shown in Figure 1b compared to the SLG reference sample without Sn nanostructures (see Figure 4). As a facile demonstration of concept, two pieces of conductive carbon tape with Al foil on the top (for better probe contacts) are used as the electrodes of the SLG photoconductor devices. Such a photoconductor device has been proved to be Ohmic from the I – V curve in Figure S6. Laser beams at $\lambda = 1550$ nm (the most important optical communication wavelength) and 650 nm (red laser) are chopped at 300 Hz to measure the photocurrent more precisely using a lock-in method (Figure 4a). The distance between the electrodes is ~ 1 cm, and the incident laser beam spots are within the SLG region. Only the photocurrent is amplified and recorded by a lock-in amplifier using this approach. The chopping frequency of 300 Hz also prevents any laser heating effect that could induce photothermal effect in the device. Under the 1550 nm laser excitation (~ 1 mW power), the Sn/SLG/quartz sample shows 5x enhancement (Figure 4b) in photoconductance. The error bars in the photocurrent reflect the noise levels due to the relatively high dark conductance of the SLG itself. On the other hand, under the 650 nm red laser excitation (~ 2 mW), the photoconductance in the Sn nanodots/SLG region is only 1.6x larger than that of the SLG/quartz (Figure 4c). These are both consistent with the data in Figure 1b showing much stronger absorption enhancement at the wavelength of 1550 nm than 650 nm. Quantitatively, though, the photocurrent enhancement is less than the optical absorption enhancement shown in Figure 1c. Such a difference is mainly attributed to the surface recombination of electron–hole pairs³⁸ at Sn nanodots/SLG interfaces, which reduces the carrier lifetime compared to case of pristine SLG/quartz reference. To overcome this issue, we proposed to insert a single-layer hexagonal boron nitride (h-BN) between the Sn nanodots and the SLG in our future work. The h-BN will act as a passivation layer for the SLG due to its extremely wide band gap (~ 6.0 eV³⁹), thereby minimizing the surface recombination. Overall, the results above clearly indicate that the enhanced optical absorption in SLG leads to increased photoconductance in our devices.

The current device does not involve any lithography process. It serves as a facile demonstration of concept for highly effective, broad-band photon management using ultrahigh refractive index nanostructures, and has plenty of room for drastic improvement toward practical applications. The relatively small photoconductance is mainly limited by the short excess carrier lifetime in SLG (\sim ps from ultrafast pump–probe spectroscopy)⁴⁰ versus a large spacing between the electrodes (~ 1 cm). It could be dramatically improved by using interdigitated electrode structures with micron-scale finger spacing since the photoconductance is given by³⁸

$$\sigma_{\text{ph}} = \frac{P}{h\nu} A (\tau_e \mu_e + \tau_h \mu_h) q \frac{1}{L^2} \quad (2)$$

Here P is the incident optical power, $h\nu$ is the photon energy, A is the absorption in SLG (see Figure 1c), τ_e and τ_h are the lifetimes of the electrons and holes, μ_e and μ_h are the mobilities of the electrons and holes, q is the electron charge, and L is the distance between the two electrodes. As L decreases from 1 cm to 1 μm , the photoconductivity can be increased by a factor of 10^8 . With further optimization of the Sn nanostructures and coupling with back reflectors, it is also promising to achieve a much higher IR absorption, especially considering that the incident IR light is already effectively scattered to oblique angles after being funneled through the nanoscale gaps between the Sn nanodots (see Figure 3c).

Interestingly, we also estimated a relatively long photo-generated carrier lifetime in CVD growth SLG from our photoconductance measurement. For the 1550 nm excitation, using $P = 1$ mW, $L = 1$ cm, $\mu_e \sim \mu_h \sim 1000$ $\text{cm}^2/(\text{V}\cdot\text{sec})$ (from Hall effect measurements), and $A \sim 15\%$ for the Sn nanodots/SLG region (Figure 1c), we find $\tau_e + \tau_h \sim 25$ ns. The corresponding injection level is $\Delta n = \Delta p \sim 10^7$ cm^{-2} . This lifetime is much longer than what was reported from femtosecond pump–probe spectroscopy,⁴⁰ which is on the order of ps. This difference is most likely due to a much lower injection level in our case since the lifetime is roughly inversely proportional to the injected carrier density. Indeed, the measured lifetime is on the same order as the theoretical prediction for an injection level of 10^7 cm^{-2} in graphene.⁴¹

CONCLUSIONS

We have demonstrated highly effective IR light trapping and photon management in SLG using self-assembled, pseudoperiodic ultrahigh refractive index Sn semimetal pseudoperiodic nanostructures. The optical absorption in SLG is strongly increased from $<1.5\%$ to $>15\%$ in a very broad IR spectral regime of $\lambda = 900$ – 2000 nm, a significant advantage over the narrow-band plasmonics enhancement of Au and Ag nanostructures. The strong near field electromagnetic interactions at the Sn nanodots/SLG interface make a dominant contribution to such an effective IR absorption enhancement. The enhanced optical absorption in SLG has also been successfully confirmed by field-enhanced Raman scattering from SLG under excitations at $\lambda = 532$, 633, and 780 nm, as well as a $5\times$ increase in photoconductance under optical excitation at $\lambda = 1550$ nm. The self-assembled pseudoperiodic Sn nanostructures also feature facile fabrication and no detrimental effect on the 2D lattice of SLG. The device performance could be further improved by coupling with backside reflectors and reducing the interelectrode spacing. The straightforward fabrication process and the promising optoelectronic performance of the Sn nanodot/SLG photonic structures could benefit the future development of 2D photonics and optoelectronics significantly. This work also opens the door to the investigations of ultrahigh refractive index semimetal nanostructures for highly effective, broad-band nanoscale photon management.

METHODS

Self-Assembly of Ultrahigh Refractive Index Pseudo-Periodic Sn Nanostructures. The self-assembled pseudoperiodic Sn nanostructures are fabricated by thermal evaporation using Lab18 Physical Vapor Deposition (PVD)

system produced by Kurt J. Lesker Company. The chamber is pumped to a based vacuum of 5×10^{-8} Torr. The evaporation source material, Sn, is provided by Kurt J. Lesker company with 99.99% purity. The substrates are kept rotating at 20 rounds per minute during the entire evaporation process to avoid nonuniformity in the thin film growth. The substrate temperatures are controlled at ~ 25 °C by chilled water. Basically, the morphology of the evaporated Sn nanostructures is controlled by the nominal thickness of the deposition process as well as the deposition rate, both read by quartz crystal monitors during deposition. The typical deposition rate of Sn is ~ 0.12 Å/s. The self-assembly of thermally evaporated Sn nanostructures on various substrates is easier than other metals, such as Al. This behavior is attributed to the much lower melting point of Sn that leads to higher surface diffusivity to form thermodynamically stable structures. In our case, the dewetting of Sn on various surfaces leads to Sn nanodot growth similarly to the Stranski-Krastanov mechanism.⁴²

Synthesis and Transfer of Graphene. The single layer graphene (SLG) in this research is prepared by Chemical Vapor Deposition (CVD).⁴³ A 25 μm -thick copper foil with 99.8% purity (Alfa Aesar #13382) is used as the growth substrate. The substrate is first soaked into nickel etchant (Transense, TFB) for 90s. After rinsing with DI water, the copper foil is placed in a hot wall CVD system. Before the growth, the substrate is first annealed at 1030 °C with 10 sccm H_2 flow. Subsequently, 60 sccm H_2 is induced into the chamber with 3.5 sccm methane (CH_4) for 30 min, while the system is maintained at 1030 °C.

PMMA supported transfer is used in this research.⁴⁴ PMMA (950 A9, Microchem Inc.) is first diluted in anisole with a ratio of 1:1. The diluted PMMA is then spun on the synthesized graphene on Cu foil with 2500 rpm for 1 min. Subsequently, the sample is baked at 80 °C in an oven for 1 h. The sample is floated on the Cu etchant (TFB, Transense) to remove the Cu foil. The PMMA/graphene stack is then floating on 10% HCl solution for 10 min. Next, the sample is rinsed with deionized water for several times. The fused quartz substrate is then used to scoop out the PMMA/graphene stack, and the sample is initially bake at 80 °C for over 8 h, followed by oven baking at 130 °C for 20 min. To remove the PMMA film, the sample is soaked in acetone at room temperature for more than 1 h. Annealing process is finally conducted to remove the PMMA residual by using 200 sccm H_2 and 200 sccm Ar mixing gas flow at 350 °C for 2 h.

Morphological Characterization. Veeco/Digital Instruments Dimension 3100 Atomic Force Microscopy (AFM) is used in the morphological characterizations, that is, Figure 1a. Tapping mode is used in all cases. Statistical data of the diameters of Sn nanodots and the gaps between the Sn nanodots (i.e., Figure S3) are obtained by fast Fourier transform (FFT). The results have been further confirmed by manually collecting 120 diameter/gap data points on the AFM images of each sample.

Optical Characterization. The transmittance and reflectance spectra from $\lambda = 300$ to 2500 nm are measured by a Jasco V-570 spectrometer equipped with a Jasco ISN-470 integrating sphere; the spectra at $\lambda > 2500$ nm are measured by a Jasco 4100 Fourier Transform Infrared (FTIR) spectrometer equipped with a Pike IR integrating sphere. The absorption is calculated by

$$\text{absorption} = 1 - \text{transmittance} - \text{reflectance} \quad (1a)$$

For the samples with 12 nm nominal thickness of Sn, the absorption in SLG is calculated by the absorption difference between the region with and without SLG, that is,

$$\begin{aligned} \text{absorption}(\text{SLG}) &= \text{absorption}(\text{Sn/SLG/quartz}) \\ &\quad - \text{absorption}(\text{Sn/quartz}) \end{aligned} \quad (2a)$$

This is based upon the fact that the Sn nanodot morphologies on SLG and on quartz are identical. Therefore, the difference can be considered as the absorption of SLG under the Sn nanodots. This method is further supported by the Raman analyses showing no absorption enhancement in the Sn nanostructures on SLG versus on quartz.

■ ASSOCIATED CONTENT

Supporting Information

The Supporting Information is available free of charge on the ACS Publications website at DOI: 10.1021/acsphotonics.8b01370.

Supporting figures (PDF).

■ AUTHOR INFORMATION

Corresponding Authors

*E-mail: jingkong@mit.edu.

*E-mail: jifeng-liu@dartmouth.edu.

ORCID

Haozhe Wang: 0000-0001-5123-1077

Jing Kong: 0000-0003-0551-1208

Jifeng Liu: 0000-0003-4379-2928

Author Contributions

*S.F. and H.W. contributed equally to this work.

Notes

The authors declare no competing financial interest.

■ ACKNOWLEDGMENTS

This work has been sponsored by National Science Foundation under the collaborative research Awards #1509272 and #1509197. We greatly appreciate the help from Dr. Charles Daghljan with the Electron Microscope Facility at Dartmouth College. We thank Dr. Christopher Levey for helpful discussions.

■ REFERENCES

- (1) Geim, A. K.; Novoselov, K. S. The rise of graphene. *Nat. Mater.* **2007**, *6*, 183–191.
- (2) Mak, K. F.; Ju, L.; Wang, F.; Heinz, T. F. *Solid State Commun.* **2012**, *152*, 1341–1349.
- (3) Nair, R. R.; Blake, P.; Grigorenko, A. N.; Novoselov, K. S.; Booth, T. J.; Stauber, T.; Peres, N. M. R.; Geim, A. K. Fine Structure Constant Defines Visual Transparency of Graphene. *Science* **2008**, *320* (5881), 1308.
- (4) Spinelli, P.; Hebbink, M.; Waele, R. D.; Black, L.; Lenzmann, F.; Polman, A. Optical Impedance Matching Using Coupled Plasmonic Nanoparticle Arrays. *Nano Lett.* **2011**, *11* (4), 1760–1765.
- (5) Atwater, H. A.; Polman, A. Plasmonics for Improved Photovoltaic Devices. *Nat. Mater.* **2010**, *9*, 205–213.
- (6) Brongersma, M. L.; Cui, Y.; Fan, S. Light Management for Photovoltaics Using High-Index Nanostructures. *Nat. Mater.* **2014**, *13*, 451–460.
- (7) Liu, J.; Liu, N.; Li, J.; Li, X. J.; Huang, J. Enhanced Absorption of Graphene with One-Dimensional Photonic Crystal. *Appl. Phys. Lett.* **2012**, *101*, No. 052104.

- (8) Zheng, G.; Zhang, H.; Xu, L.; Liu, Y. Enhanced Absorption of Graphene Monolayer with a Single-Layer Resonant Grating at the Brewster Angle in the Visible Range. *Opt. Lett.* **2016**, *41* (10), 2274–2277.
- (9) Khaleque, A.; Hattori, H. T. Absorption Enhancement in Graphene Photonic Crystal Structures. *Appl. Opt.* **2016**, *55* (11), 2936–2942.
- (10) Yan, H.; Low, T.; Zhu, W.; Wu, Y.; Freitag, M.; Li, X.; Guinea, F.; Avouris, P.; Xia, F. Damping Pathways of Mid-Infrared Plasmons in Graphene Nanostructures. *Nat. Photonics* **2013**, *7*, 394–399.
- (11) Deng, B.; Guo, Q.; Li, C.; Wang, H.; Ling, X.; Farmer, D. B.; Han, S.; Kong, J.; Xia, F. Coupling-Enhanced Broadband Mid-Infrared Light Absorption in Graphene Plasmonic Nanostructures. *ACS Nano* **2016**, *10* (12), 11172–11178.
- (12) Qin, C.; Wang, B.; Huang, H.; Long, H.; Wang, K.; Lu, P. Low-Loss Plasmonic Supermodes in Graphene Multilayers. *Opt. Express* **2014**, *22* (21), 25324–25332.
- (13) Hashemi, M.; Farzad, M. H.; Mortensen, N. A.; Xiao, S. Enhanced Absorption of Graphene in the Visible Region by Use of Plasmonic Nanostructures. *J. Opt.* **2013**, *15* (5), No. 055003.
- (14) Lu, H.; Cumming, B. P.; Gu, M. Highly Efficient Plasmonic Enhancement of Graphene Absorption at Telecommunication Wavelengths. *Opt. Lett.* **2015**, *40* (15), 3647–3650.
- (15) Liu, Y.; Cheng, R.; Liao, L.; Zhou, H.; Bai, J.; Liu, G.; Liu, L.; Huang, Y.; Duan, X. Plasmon Resonance Enhanced Multicolour Photodetection by Graphene. *Nat. Commun.* **2011**, *2*, 579.
- (16) Svetovoy, V. B.; Palasantzas, G. Graphene-on-Silicon Near-Field Thermophotovoltaic Cell. *Phys. Rev. Appl.* **2014**, *2*, No. 034006.
- (17) Smith, P. J. *Chemistry of Tin*, 2nd ed.; Springer Science + Business Media: University College, London, U.K., 1998.
- (18) Sant, S.; Schenk, A. Band-Offset Engineering for GeSn-SiGeSn Hetero Tunnel FETs and the Role of Strain. *IEEE J. Electron Devices Soc.* **2015**, *3* (3), 164–175.
- (19) Hagemann, H.-J.; Gudat, W.; Kunz, C. Optical Constants from the Far Infrared to the X-Ray Region: Mg, Al, Cu, Ag, Au, Bi, C, and Al₂O₃. *J. Opt. Soc. Am.* **1975**, *65* (6), 742–744.
- (20) Fox, T. J.; Howson, R. P.; Emmony, D. C. Optical Properties of Thin Films of Antimony. *J. Phys. D: Appl. Phys.* **1974**, *7* (13), 1864–1872.
- (21) Baranov, D. G.; Zuev, D. A.; Lepeshov, S. I.; Kotov, O. V.; Krasnok, A. E.; Evlyukhin, A. B.; Chichkov, B. N. All-dielectric Nanophotonics: The Quest for Better Materials and Fabrication Techniques. *Optica* **2017**, *4* (7), 814–825.
- (22) Takeuchi, K.; Adachi, S. Optical Properties of β -Sn Films. *J. Appl. Phys.* **2009**, *105* (7), No. 073520.
- (23) Wang, X.; Wong, A.; Malek, S.; Cai, Y.; Liu, J. High-Performance Infrared Light Trapping in Nano-Needle Structured p+ SnO_x ($x \leq 1$)/Thin Film n-Ge Photodiodes on Si. *Opt. Lett.* **2015**, *40* (11), 2603–2606.
- (24) Wong, A.; Wang, X.; Liu, J. Nano-Needle Structured, Ambipolar High Electrical Conductivity SnO_x ($x \leq 1$) Thin Films for Infrared Optoelectronics. *J. Appl. Phys.* **2015**, *117*, 103109.
- (25) Anderson, P. A.; Schmidt, B. S.; Lipson, M. High Confinement in Silicon Slot Waveguides with Sharp Bends. *Opt. Express* **2006**, *14* (20), 9197–9202.
- (26) Barrios, C. A.; Sánchez, B.; Gylfason, K. B.; Griol, A.; Sohlström, H.; Holgado, M.; Casquel, R. Demonstration of Slot-Waveguide Structures on Silicon Nitride/Silicon Oxide Platform. *Opt. Express* **2007**, *15* (11), 6846–6856.
- (27) Campion, A.; Kambhampati, P. Surface-Enhanced Raman Scattering. *Chem. Soc. Rev.* **1998**, *27*, 241–250.
- (28) Oliinyk, H. Pressure Dependence of Raman Phonons of Metallic β -Sn. *Phys. Rev. B: Condens. Matter Mater. Phys.* **1992**, *46* (10), 6589–6591.
- (29) Das, A.; Pisana, S.; Chakraborty, B.; Piscanec, S.; Saha, S. K.; Waghmare, U. V.; Novoselov, K. S.; Krishnamuethy, H. R.; Geim, A. K.; Ferrari, A. C.; Sood, A. K. Monitoring Dopants by Raman Scattering in an Electrochemically Top-Gated Graphene Transistor. *Nat. Nanotechnol.* **2008**, *3*, 210–215.
- (30) Wang, F.; Zhang, Y.; Tian, C.; Girit, C.; Zettl, A.; Crommie, M.; Shen, Y. R. Gate-Variable Optical Transitions in Graphene. *Science* **2008**, *320* (5873), 206–209.
- (31) Chukin, G. D.; Malevich, V. I. Infrared spectra of silica. *J. Appl. Spectrosc.* **1977**, *26* (2), 223–229.
- (32) Optical Properties of Silica Glass. <https://www.crystran.co.uk/optical-materials/silica-glass-sio2>, accessed August 2018.
- (33) Dlubak, B.; Seneor, P.; Anane, A.; Barraud, C.; Deranlot, C.; Deneuve, D.; Servet, B.; Mattana, R.; Petroff, F.; Fert, A. Are Al₂O₃ and MgO Tunnel Barriers Suitable for Spin Injection in Graphene? *Appl. Phys. Lett.* **2010**, *97*, No. 092502.
- (34) Jin, Z.; Su, Y.; Chen, J.; Liu, X.; Wu, D. Study of AlN Dielectric Film on Graphene by Raman Microscopy. *Appl. Phys. Lett.* **2009**, *95*, 233110.
- (35) Wang, Z.; Wang, X.; Liu, J. An Efficient Nanophotonic Hot Electron Solar-Blind UV Detector. *ACS Photonics* **2018**, *5* (10), 3989–3995.
- (36) Sheng, X.; Liu, J.; Kozinsky, I.; Agarwal, A. M.; Michel, J.; Kimerling, L. C. Design and Non-Lithographic Fabrication of Light Trapping Structures for Thin Film Silicon Solar Cells. *Adv. Mater.* **2011**, *23* (7), 843–847.
- (37) Siegfried, T.; Ekinci, Y.; Martin, O. J. F.; Sigg, H. Gap Plasmons and Near-Field Enhancement in Closely Packed Sub-10 nm Gap Resonators. *Nano Lett.* **2013**, *13* (11), 5449–5453.
- (38) Sze, S. M. *Physics of Semiconductor Devices*, 2nd ed.; John Wiley & Sons: Hoboken, New Jersey, U.S.A., 1998.
- (39) Kim, K. K.; Hsu, A.; Jia, X.; Kim, S. M.; Shi, Y.; Hofmann, M.; Nezich, D.; Rodriguez-Nieva, J. F.; Dresselhaus, M.; Palacios, T.; Kong, J. Synthesis of Monolayer Hexagonal Boron Nitride on Cu Foil Using Chemical Vapor Deposition. *Nano Lett.* **2012**, *12* (1), 161–166.
- (40) Limmer, T.; Feldmann, J.; Como, E. D. *Phys. Rev. Lett.* **2013**, *110*, 217406.
- (41) Rana, F. Electron-Hole Generation and Recombination Rates for Coulomb Scattering in Graphene. *Phys. Rev. B: Condens. Matter Mater. Phys.* **2007**, *76*, 155431.
- (42) Eisenmenger-Sittner, C.; Bangerta, H.; Störi, H.; Brenner, J.; Barnac, P. B. Stranski–Krastanov Growth of Sn on a Polycrystalline Al Film Surface Initiated by the Wetting of Al by Sn. *Surf. Sci.* **2001**, *489* (1–3), 161–168.
- (43) Reina, A.; Jia, X.; Ho, J.; Nezich, D.; Son, H.; Bulovic, V.; Dresselhaus, M. S.; Kong, J. Large Area Few-Layer Graphene Films on Arbitrary Substrates by Chemical Vapor Deposition. *Nano Lett.* **2009**, *9* (1), 30–35.
- (44) Wang, H.; Leong, W. S.; Hu, F.; Ju, L.; Su, C.; Guo, Y.; Li, J.; Li, M.; Hu, A.; Kong, J. Low-Temperature Copper Bonding Strategy with Graphene Interlayer. *ACS Nano* **2018**, *12* (3), 2395–2402.